SWEA FM2 calibration report

Version 5.1 November, 18, 2005

Andrei Fedorov, Jean-Louis Médale, Claude Aoustin,Jean Rouzaud,
Jean-André Sauvaud

Centre d'Etude Spatiale des Rayonnements (CESR)
Toulouse, France

Content

1. Principal design and theoretical properties of the sensor

The SWEA analyzer optics is shown in Figure 1. The properties of the analyzer calculated analytically are as follows:

1. The K factor which is the ratio of the energy per charge of the electrons *E/Q* [eV/<electron charge>] to the potential of the inner hemisphere *Uan* [V] :

$$K = \frac{E/Q}{Uan} = \frac{R1}{2.(R2 - R1)} = 6.7$$

2. The aperture area:

$$S = \frac{2}{3}.(R2 - R1).2\theta.R1 = 0.45 \text{ cm}^2$$

3. The normalized velocity space volume (expressed as the product of the energy resolution by the width of the elevation acceptance angle:

$$\left\langle \frac{\Delta E}{E} \Delta\alpha \right\rangle = \frac{1}{2}\left(\frac{R2 - R1}{R1} \right)^2 \csc^3\left(\frac{90 - \sigma}{2} \right)\left(\frac{7}{8} + \cos\left(\frac{90 - \sigma}{2} \right) \right) = 0.017 \text{ rad.eV/eV}$$

4. The total geometrical factor for the 360° field of view:

$$GF = 4\pi.\frac{2}{3}.\left\langle \frac{\Delta E}{E}.\Delta\alpha \right\rangle.(R2 - R1).R1.\theta = 0.033 \text{ cm}^2.\text{sr.eV/eV}$$

Numerical simulations of the sensor give results quite close to the analytical one, as displayed in Table 1 (see Annex 4 for a detailed description of the simulation results):

Elevation,	K	ΔE/E	GF, cm^2.sr.eV/eV
-54.9	6.38	0.137	3.23E-02
-48.3	6.35	0.181	4.26E-02
-40.3	6.33	0.180	4.09E-02
-21.8	6.39	0.187	3.72E-02
1.1	6.36	0.176	3.32E-02
19.4	6.36	0.170	3.86E-02
41.6	6.27	0.173	3.88E-02
52.8	6.24	0.143	2.80E-02
61.1	6.19	0.119	1.18E-02

Table 1 : *Summary table of the results of the numerical simulations of SWEA*

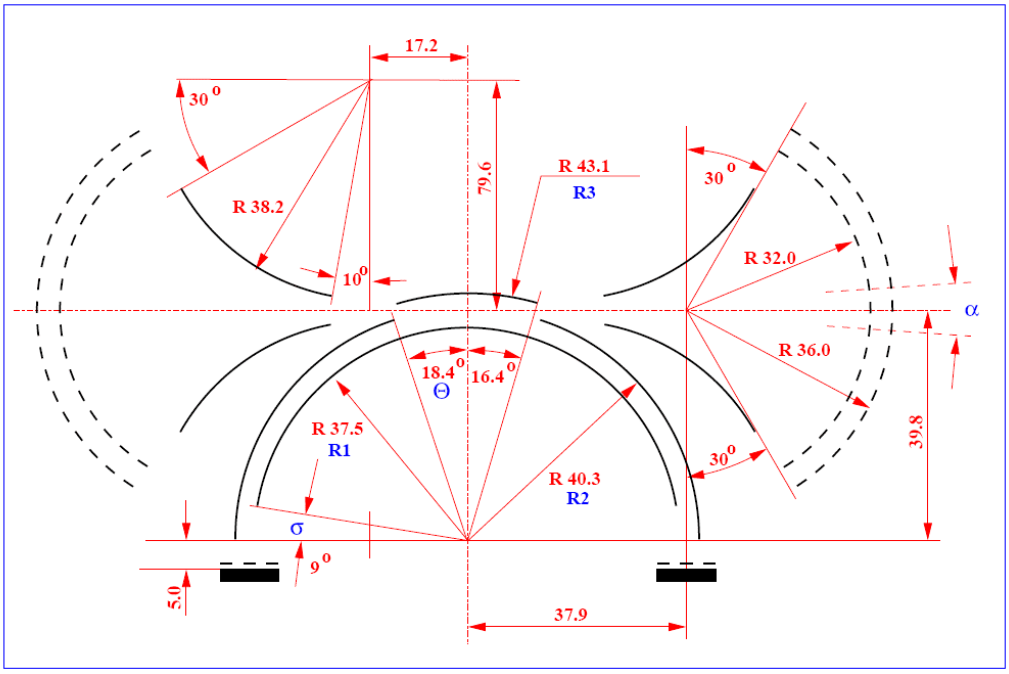

Figure 1: *Electrostatic optics of the SWEA sensor. The main dimensions used to calculate the analyzer properties are marked in blue. α is the elevation angle acceptance range.*

2. Electrical setup and calibration constants

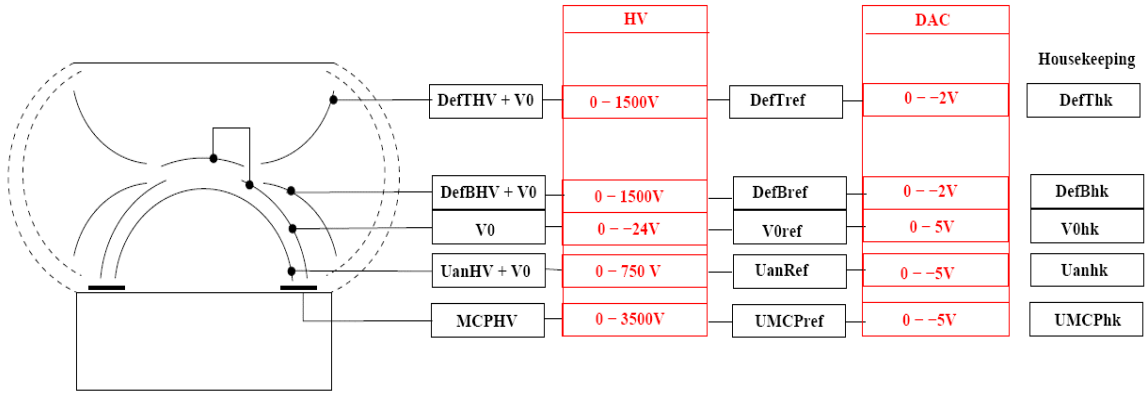

Figure 2: *Electrical block diagram of the SWEA calibration setup. The DAC is located outside of the vacuum chamber. The DAC resolution is 0.lmV. All housekeeping values are recorded with an accuracy of 0.1 mV.*

The electrical setup is shown in Figure 2. The correspondence of reference, high voltage, and housekeeping values is as follows:

$V0$ [V] = -5.000×10^{-3} $V0ref$ [mV] - 1.366×10^{-3}

$V0$ [V] = -5.001×10^{-3} $V0hk$ [mV] + 1.796×10^{-3}

$UanHV$ [V] = -1.503×10^{-1} $UanRef$ [mV] + 2.222×10^{-2} + $V0$

$UanHV$ [V] = 0.1689 $Uanhk$ [mV] - 0.1236

$UdefTHV$ [V] = -0.7467 $UdefTref$ [mV] + 0.2545 + $V0$

$UdefTHV$ [V] = 0.3311 $UdefThk$ [mV] + 0.1835

$UdefBHV$ [V] = -0.7540 $UdefBref$ [mV] + 0.0249 + $V0$

$UdefBHV$ [V] = 0.3349 $UdefBhk$ [mV] - 0.0125

$MCPHV$ [V] = -0.687 $UMCPref$ [mV] + 18.22

$MCPHV$ [V] = 1.003 $UMCPhk$ [mV] - 2.25

(Note that these calibration values are valid for $T = 20°C$).

3. MCP gain and dead-time

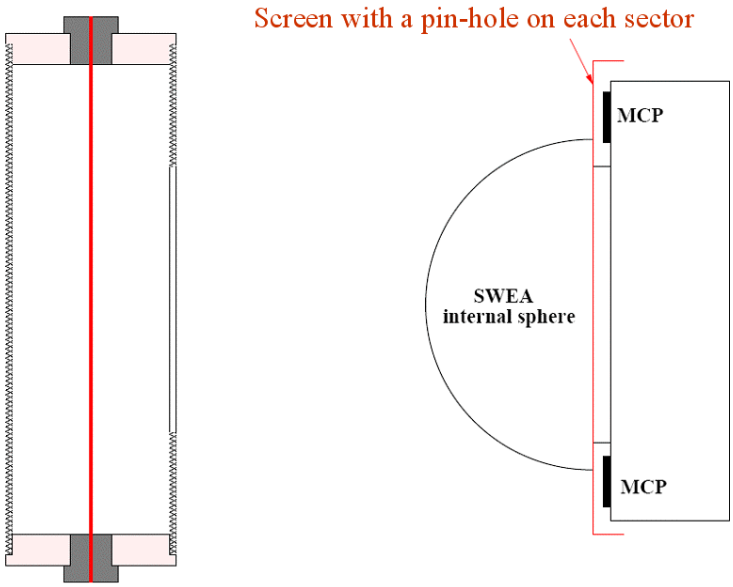

Figure 3: *Setup for MCP characterization. Pin-holes of 0.5mm diameter are located at 76.6mm firom the center of the sensor, in the middle of each azimuthal sector. The gun has been moved in vertical and horizontal directions to illuminate each sector successively. The total current collected on the cylinder surrounding the gun and by a CEM is use to control the beam intensity. The beam dynamics is* 10^3.

The setup for the characterization of the MCP is shown in Figure 3. The electron beam is narrow in the *Y* direction and has a non-uniform (even multi-peaked) distribution in the *Z* direction. It is worth to note that the shape of the distribution is independent of the total electron current (see Annex l for details). The gun can be moved along *Y* and *Z* to illuminate each pinhole (see Figure 7). The total electron current of the beam is *Jbeam* = *Jmeas* × 0.0127. Here *Jmeas* is the current emitted by the gun and collected on the surrounding cylinder.

MCP gain

The count rate of each MCP sector versus *MCPHV* value is shown in Figure 4. Subsequent SWEA calibration has been made with *MCPHV* = 2800 *V*.

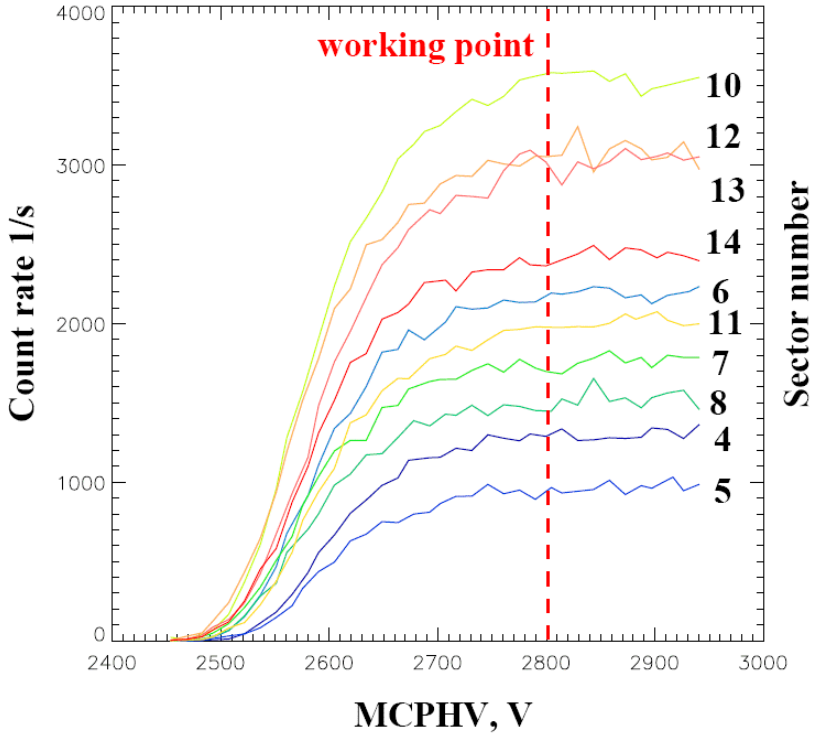

Figure 4: *Count versus MCPHV[V] for selected MCP sectors. The vertical dashed line shows the working point for the subsequent calibrations. The saturation level of each MCP sector is different due to the different beam intensities used for these measurements.*

Dead-time

The spatial distribution of the electron current produced by the gun does not change when the total flux is increasing. We use this gun property to measure the MCP dead-time. The electron beam has been swept along the Z and Y axis. At each point, both the MCP sector count rate and the electron current have been measured. Each MCP sector has been illuminated through a 0.5mm diameter pin-hole. Since the diameter of a single MCP channel is 12.5 μm and the relative channel area is 0.6, the number of illuminated channels is 978.

The method of measurements is as follows:

1. Set a low total electron beam current (J_{meas}= 2pA)

2. Find the beam spatial distribution by scanning the beam around each sector's pinhole.

3. Reconstruct the incident electron current per MCP single channel as follows:

$$\Phi_r = \frac{J_{meas} \times 1.6 \times 10^{-24} \times 0.0127}{\sum Count_{low}(Y,Z) / S_{hole} \times \Delta Y . \Delta Z} \times Count_{low}(Y,Z)/978 \qquad (1)$$

$\Phi_r(Y,Z)$ is the reconstructed incident electron current per single MCP channel [s^{-1}](i.e. electrons/s), $Count_{low}(Y,Z)$ is the measured count rate when the gun current is low [s^{-1}], ΔY and ΔZ are the sweep steps. Here we assume, that $Count_{low}(Y, Z)$ is well below the channel saturation level. Thus the reconstruction for the low gun current allows to define the MCP efficiency to be equal to 0.83.

4. Set a high total electron beam current (J_{meas}= 150 pA)

5. Repeat the measurements. The count profiles normalized by the gun current versus *Y* and versus *Z* are shown in Figure 5. I this case of high gun current, the count rate is saturated.

6. Then, assuming that the real spatial distribution of the electron current do not change, the incident current per channel was reconstructed using (1). Such reconstructed current versus the measured count rate of a single channel is shown in Figure 6.

In a simple dead-time model the real count rate Φ is:

$$\Phi = \frac{C}{1 - C\tau} \qquad (2)$$

Here τ is the dead-time of a single channel. The solid line in Figure 6 corresponds to a dead-time of 120ms.

Conclusions:

Minimal MCPHV:	2800 V
MCP efficiency:	0.83
Single MCP channel dead-time:	120 ms

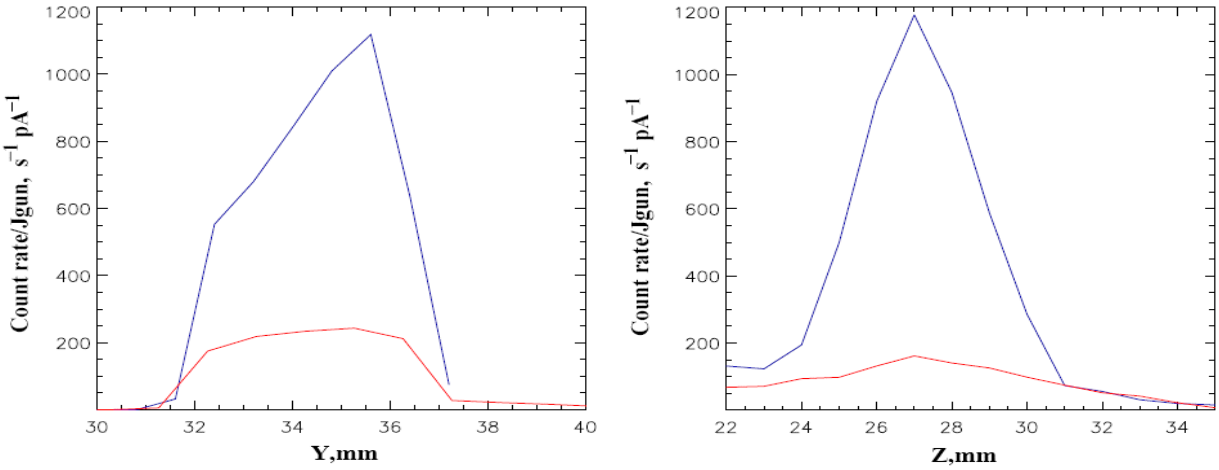

Figure 5: *Y (left panel) and Z (right panel) profiles of the sector 5 count rate normalized to the total current of the gun. The difference in the main peak values is caused by the MCP saturation effect.*

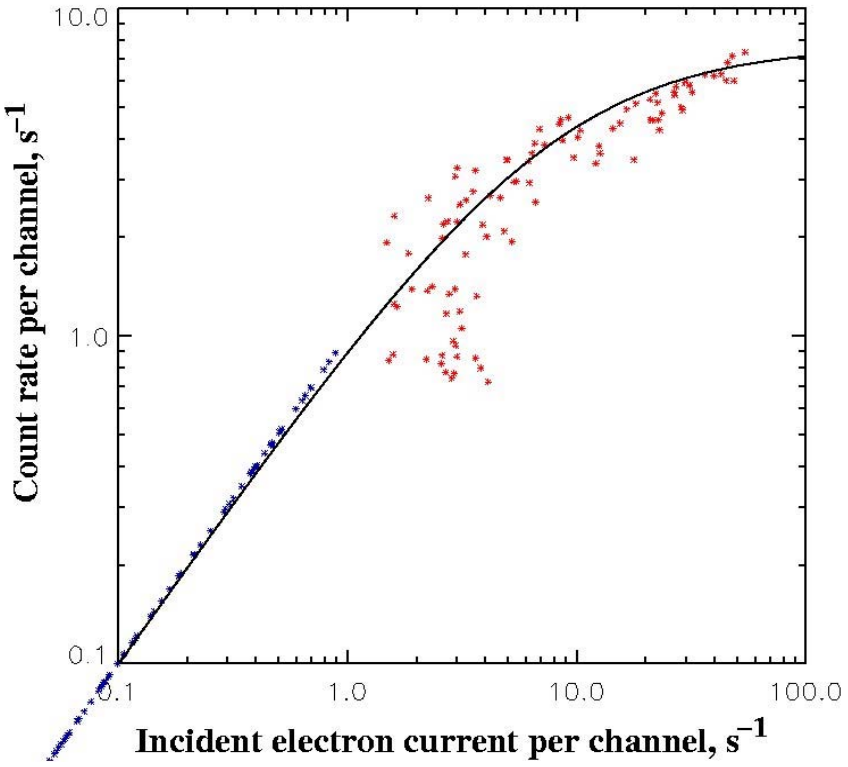

Figure 6: *MCP single channel count rate versus real incident current per MCP channel. The incident current is reconstructed from the count rate profile derived from the low current setup of the gun.*

4. Calibration setup. Mechanical coordinate system. Electron beam properties.

Here we give only a brief introduction to the SWEA calibration mechanical setups. Annex 3 furnishes detailed explanations. The general setup is shown in Figure 7. The sensor can be rotated around the Y axis and the gun can be displaced along the Z and Y axis. Actually we used two different sensor positions: 1) as shown in Figure 7 (left), called "positive" setup; 2) upside-down position when SWEA axis is anti-parallel to Z, called "negative" setup (not shown). "Positive" setup is used to investigate the upper hemisphere of the SWEA field-of-view, and "negative" setup is used to investigate the lower hemisphere of SWEA.

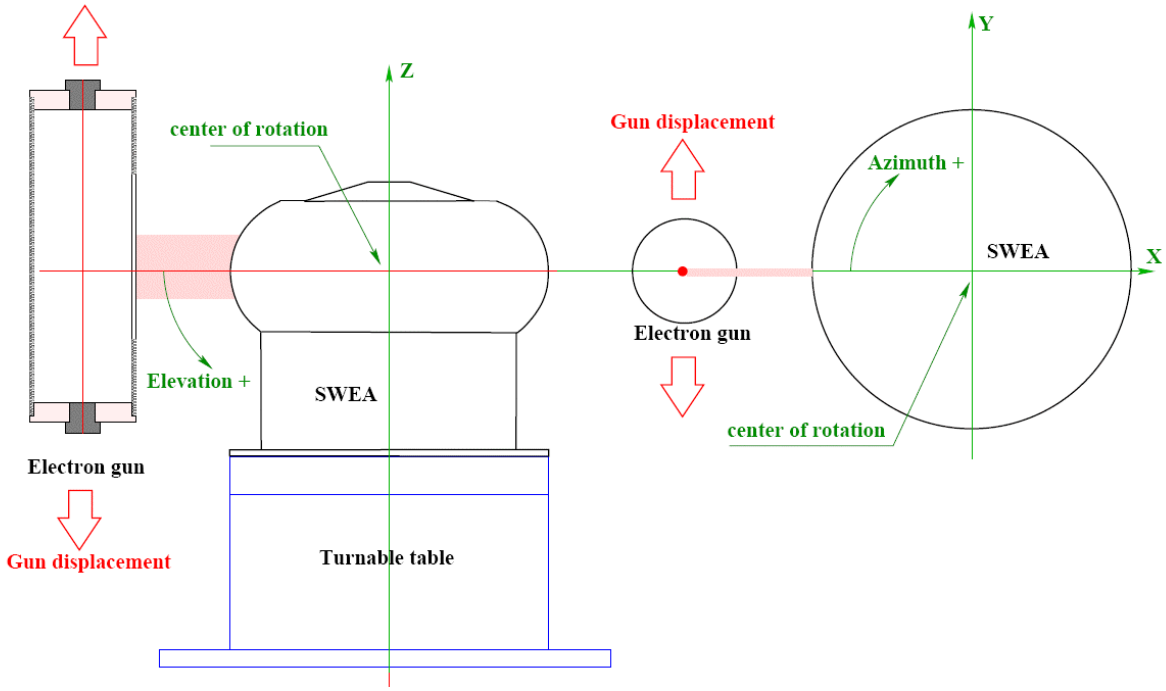

Figure 7: *Calibration setup and coordinate system for SWEA tests, (see Annex 3).*

Electron beam

The electron gun properties are described in Annex 1, Annex 2, and Annex 3. Its general properties are given below:

1. The beam is narrow in the Y direction. Its thickness can be considered as negligible.

2. The gun used for the "positive" set-up produces a parallel 2D electron beam in the XZ plane. The beam is not uniform in the Z direction. Superposing the beam for several Z positions of the gun allows to obtain a uniform beam with a linear current density of 23000 $s^{-1}.cm^{-1}.pA^{-1}$ (normalized to *Jmeas*).

The gun used for the "negative" setup produces a diverging beam with a nearly uniform normalized current density of 1400 s^{-1}. deg^{-1}. pA^{-1}. The focal point is located 137mm away from the Z axis.

4. The stability of the electron gun is about 10%. The gun flux *Jmeas* is read for each SWEA count reading.

Mechanical terms

Mechanical terms are introduced in Figures 7 and 8 as follows:

Θ_M - mechanical rotation of the instrument around Y (elevation)
Φ- mechanical azimuth equal to the beam azimuth
YGUN - gun shift from the XZ plane
ZGUN - vertical gun position.
Θ - beam elevation (see Figure 8)
Ω - latitude where the electron beam crosses the external grid of SWEA

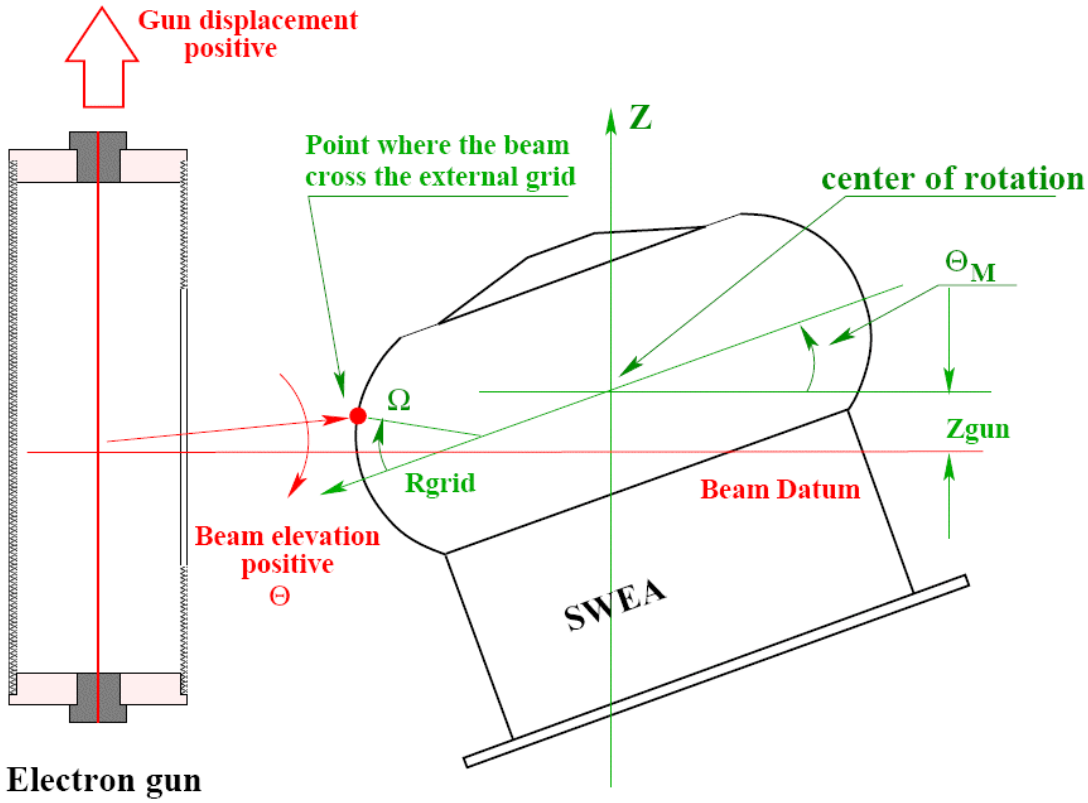

Figure 8: *Calibration scheme in the XZ plane; valid for the "negative" as well as for the "positive" setups.* Θ *is the beam elevation.* Θ_M *is the mechanical rotation angle of the sensor. The beam crosses the exterior grid of the sensor at the point defined by* Ω (the *centre of this angle is the centre of the grid curvature).*

5. Electrostatic terms, measurement scheme, and instrument response

Electrostatic terms

The electron trajectories inside the analyser are defined by the ratio

$$K = (E/Q)/Uan$$

Here *E* is the electron energy in eV, *Q* is the electron charge, (= 1), and *Uan* is the analyzer voltage. The other value defining the electron trajectories in the deflector part of the sensor is:

$$D = (UdefTHV - UdefBHV)/(E/Q)$$

Here *UdefTHV* and *UdefBHV* are the voltages applied to the top and the bottom electrodes of the deflector (see section 2). Later we will use *Udef = UdefTHV - UdefBHV*.

Measurement scheme and *E -Θ* response

Count rate versus *K* and *D* is shown in Figure 9. This distribution corresponds to a fixed beam direction and to a fixed electron energy. The electrodes voltages are swept. In reality we need to obtain the response of the instrument when *Udef = const* and *Uan = const* (or equivalently *D.K = const)* for various *E* and Θ. For a fixed Θ this corresponds to a sweep along one red trajectory in Figure 9. Note that *K* corresponds to *E* in any case. Shifting the entire distribution along *D* is equivalent to change *Θ*. Hence we can replace the mechanical Θ variations by changing the red trajectory in the *D — K* space. For *K = K0* (centre of the energy response) the transformation from *D* to *Θ* will be:

$$(\Theta-\Theta 0) = -(d\Theta/dD).(D-D0) \qquad (3)$$

dΘ/dD is obtained from the calibration (see Annex 3 for details). D0 is the center of the D response. Thus having the D-K response, we can transform it into the E-Θ response (see examples in section 6)

Geometrical factor of the sensor

For a given Φ and a given (*D.K)*, let us define G_{lin} *[cm². rad. eV/eV]* as the "azimuthal density" of the geometrical factor of the sensor, i.e. the integral of the effective aperture over *E/E0* and over the elevation angle.

For the "positive" setup:

$$G_{lin} = \{\Sigma\Sigma\ CountY(\Theta_i,K_j).(\Delta K/K0).\Delta\Theta\}/P \qquad (4)$$

Here *P* is the electron current linear density [$cm^{-1}\cdot s^{-1}$] (see section 3), Δ*K* is the *K* step of the measurement, and ΔΘ is the reconstructed virtual Θ acceptance step. *CountY* = Σ.*Count.ΔY is* the integral over the Y_{GUN} sweep (see the next section).

For the 'negative" setup:

$$G_{lin} = \{\Sigma\Sigma\ CountY(\Omega_i,K_j).(\Delta K/K0).\Delta\Omega.R_{grid}\}/P \quad (5)$$

Here *P* is the electron current angular density (see section 3), $\Delta\Omega.R_{qrid}$ is the shift of the acceptance area along the external grid of the sensor (see Annex 3 for a complete explanation). The final geometrical factor of one sector, *G F*, is the integral of G_{lin} over the sector azimuthal width.

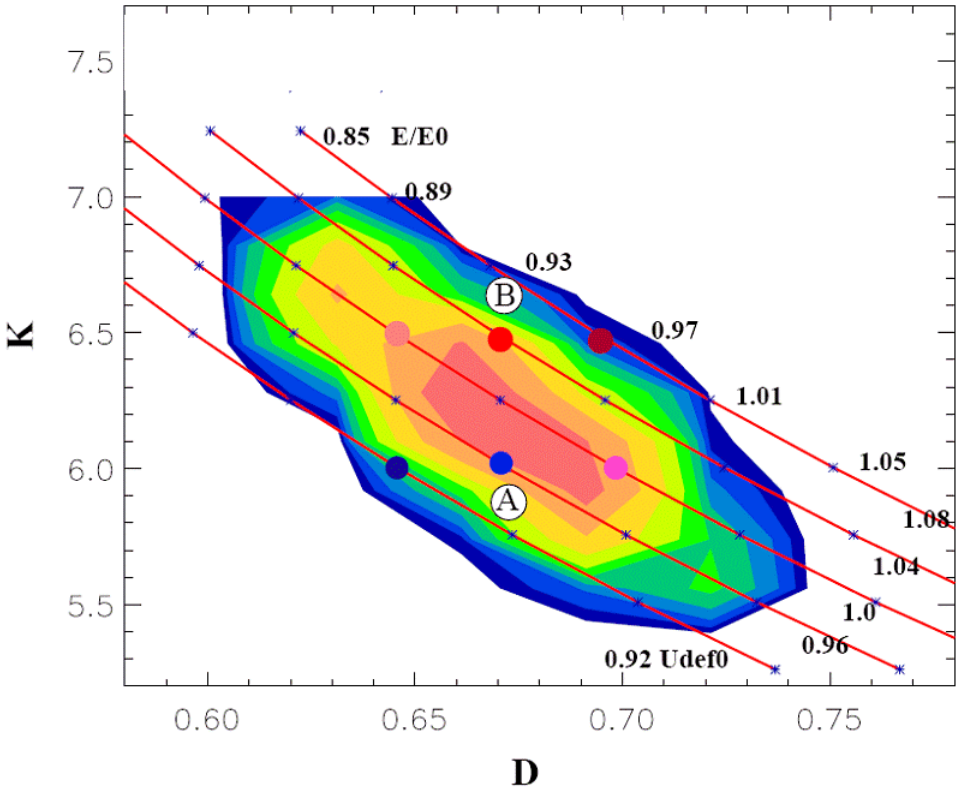

Figure 9: *Count rate distribution for Θ_M = 50°. Red lines show the Uan = const and Udef = const paths corresponding to different Udef. The corresponding E/E0 values are shown on the upper side. The Udef/Udef0 ratio is given near each red line.*

6. Master plan of the calibrations

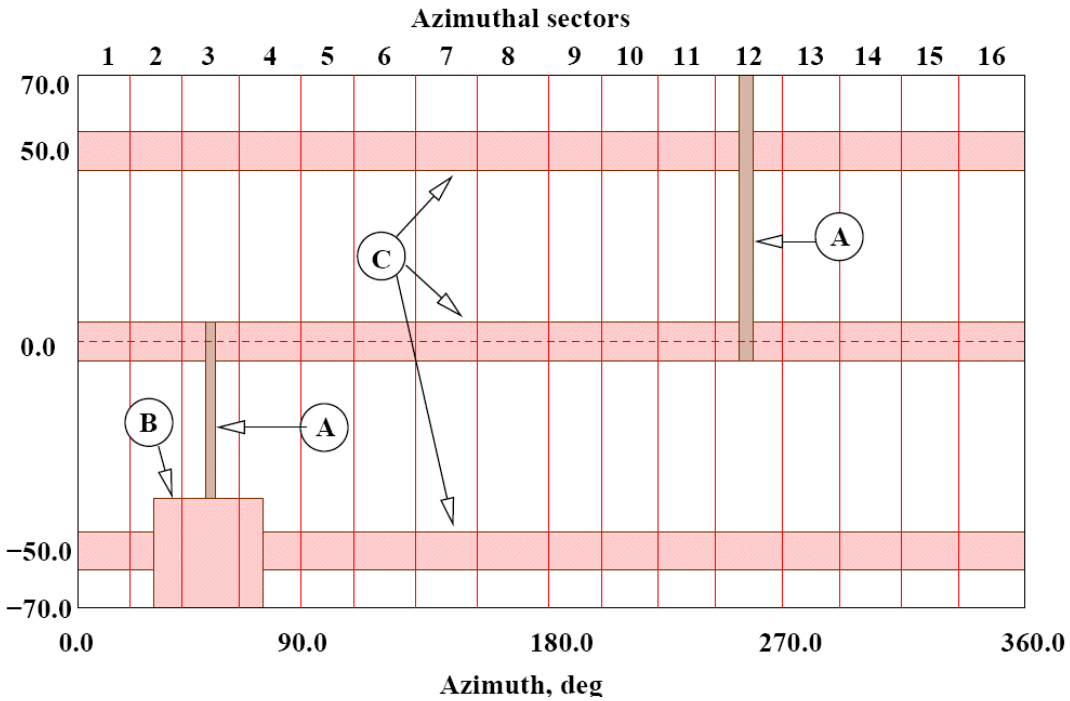

Figure 10: *Calibration master plan. Parts of the angular range of the instrument have been surveyed by different measurements mode. See text for details.*

A number of technical measurements were performed (see Annex 3) to adjust the calibration regimes to the instrument. Thus the *K, Θ, and* Φ steps and ranges have been chosen. Also the Z_{GUN} origin and the gun sweeping ranges and steps have been defined after the first test measurements (see Annex 3 for details). It is worth to note here that a change of the beam vertical position results in a change of Θ_M. Since the *Z* width of the beam is restricted, we have to keep the center of the beam distribution always at the center of the sensor aperture. An appropriate function has been obtained from the technical measurements (see Annex 3).

For the "positive" setup the Z_{GUN} compensation is:

$$Z0[\text{mm}] = 21.26 - 0.686\ \Theta_M + 0.0007\times10^{-6}\times\Theta_M^2 \qquad (6)$$

For the “negative setup”, this value is:

$$Z0[\text{mm}] = -1.4 + 0.492\times\Theta_M - 0.0032.10^{-6}\times\Theta_M^2 \qquad (7)$$

The function dΘ/dD has been measured versus D:

$$d\Theta/dD[\text{deg}] = 81.5 - 1.88\times D \qquad (8)$$

After several adjustments the following measurements have been made (see Figure 10):

A – Measurements of the elevation response with fine steps especially for the extreme elevations. These measurements have been done for a constant azimuth corresponding to the center of the azimuthal sector.

B - Measurements at the end of the elevation range with good (3°) elevation and azimuth resolutions. The azimuthal range has been covered completely at least for one sector.

C - Measurements over the entire azimuthal range with a 3° resolution, for three fixed Θ_M values. Since for positive and negative elevations different SWEA setups are used, zero mechanical elevation has been tested two times.

In each measurement mode the measurement sequence was:

1. For the given value of Θ_M do:
2. Calculate D0 using equation 10.
3. Set the $Z0_{GUN}$ gun position according to equation 6 or 7
4. For each Y_{GUN} gun position from-17.0mm to +17.0mm with a 5mm step do:
5. For a set of Z_{GUN} gun positions from $Z0_{GUN}$ = 8mm to $Z0_{GUN}$ = 7mm with a 2.5 mm step for "positive" setup and only for ZQ_{GUN} for negative setup do:
6. Measure the count rate at 13 *K* points in the interval 5.0 to 7.7 for each of 11*D* values in the interval D0 - 0.2 to D0 + 0.2
7. For the "positive" setup sum all *D* - *K* distributions taken at individual *Z* positions of the gun.
8. Integrate (trapeze method) all *D* - *K* distributions obtained for different Y_{GUN} positions (see section 6).
9. Convert each *D* - *K* distribution to the Θ - *K* one.

The complete measurement and data processing scheme is given in Annex 3.

7. Data processing and examples of sensor responses

For each individual Θ- *K* spectrum G_{lin} has been calculated. Then, using this integral value, we can transform the Θ- *K* spectrum to the effective aperture function of Θ and *K*.

Figure 11,12, and 13 show the examples of measured and simulated sensor aperture as a function of Θ and *K* measured for a fixed Φ corresponding to the middle of an anode sector.

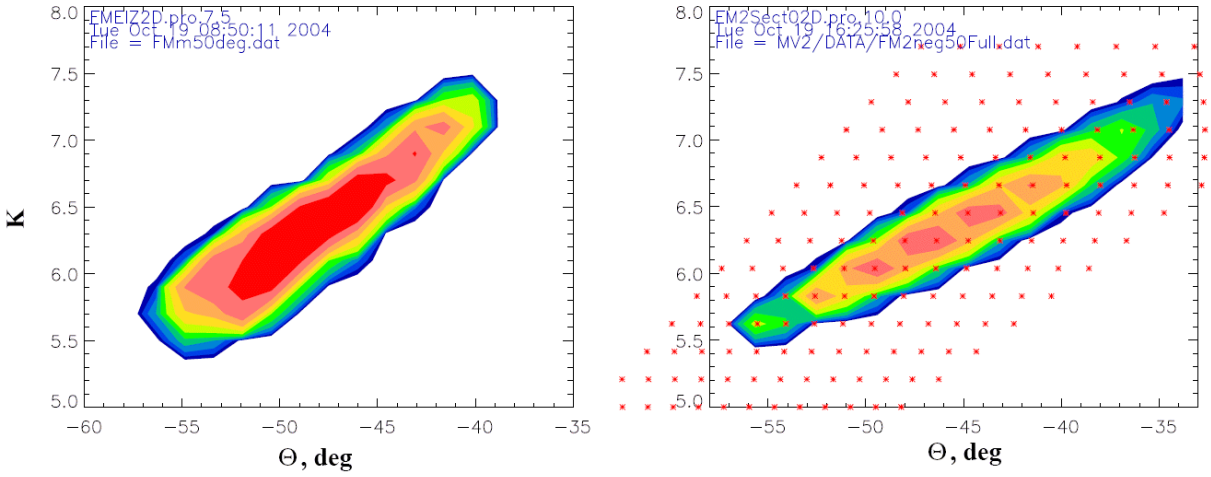

Figure 11: *2D plot of SWEA effective aperture as a function of Θ and K for D0 = -0.59. Contours are spaced by √2. The left panel shows the simulation results and the right panel shows the measurement results. Red points indicate the actual sweeping mesh.*

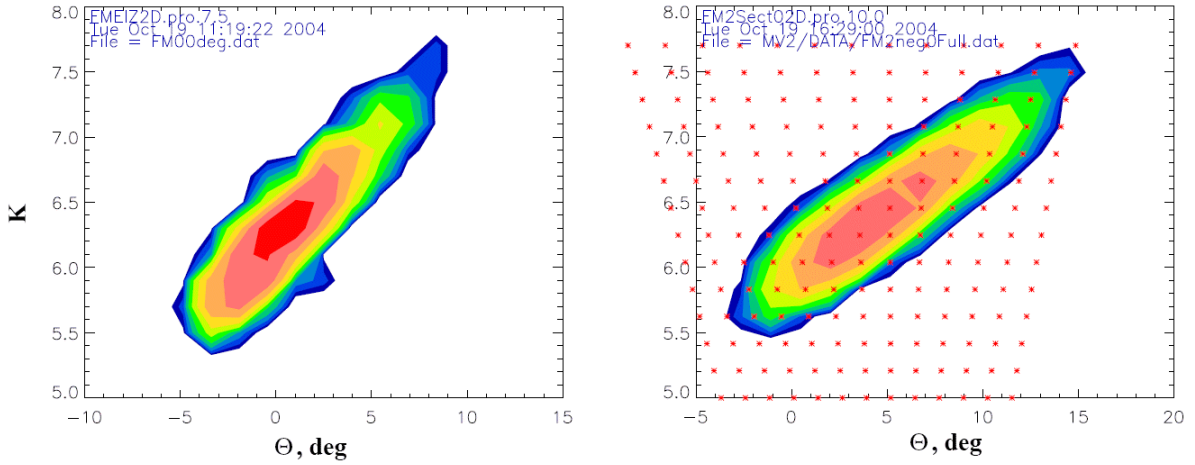

Figure 12: *Same as Figure 11 but for D0 = 9.10*$^{-3}$

The following Figures, 14 and 15, show examples of the *K*, Θ responses of the instrument in mode C and mode A respectively. These profiles are shown for measurements and simulations for a given azimuth Φ. The measured profiles are fairly consistent with the

simulation results shown by dashed curves (see Annex 4).

Conclusions:

1. The K-Θ response of the sensor is very variable with D (i.e. elevation angle);
2. The $D \Rightarrow \Theta$ reconstruction method is adequate.
3. The SWEA measured properties are generally consistent with simulation results.

The next two sections describe the complete set of the sensor properties versus elevation angle.

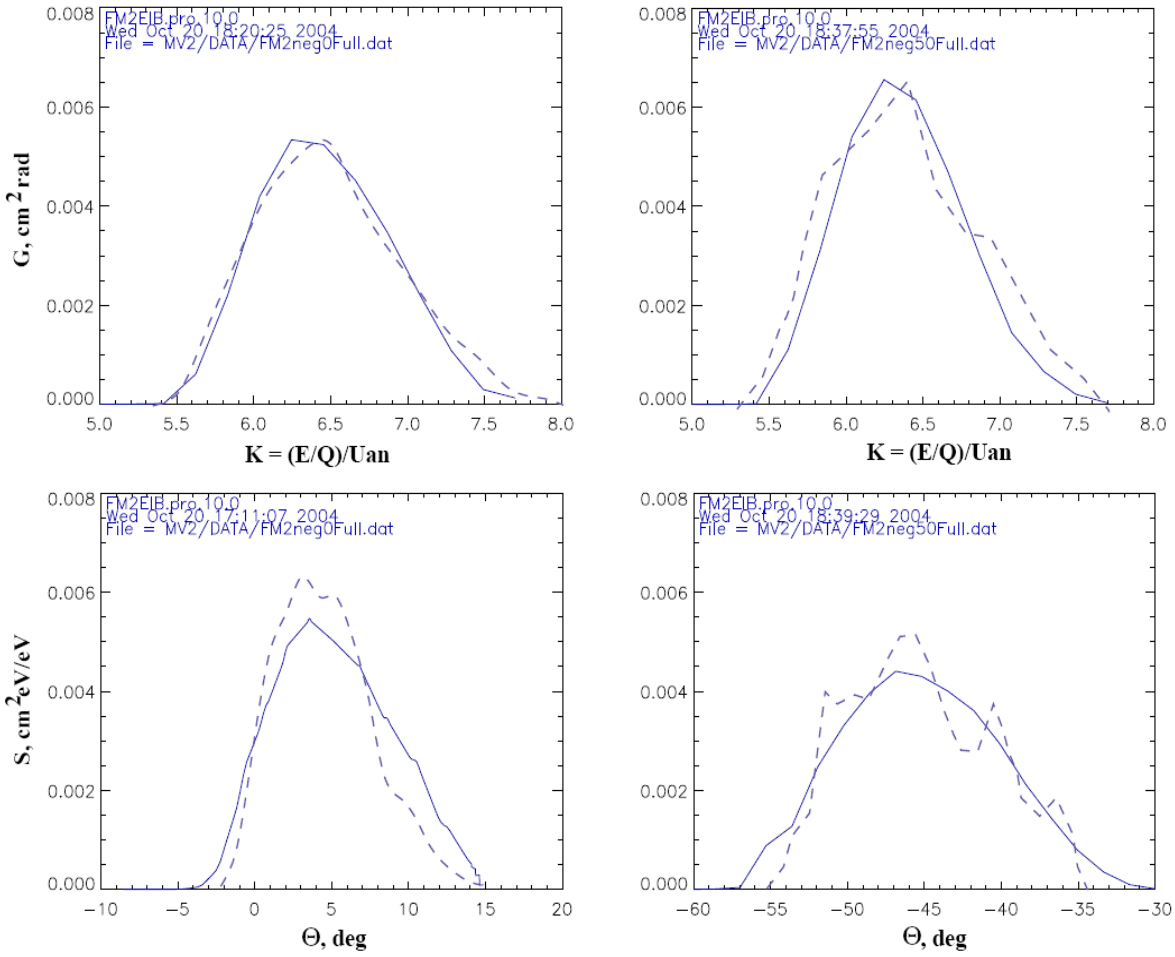

Figure 14: *Examples of the sensor responses for a specific azimuth, corresponding to the center of an azimuthal sector. Left column of the panels show properties for D = 0.028, and right panels for D = -0.707. Measurements are made for the "negative" sensor position (see Annex 3). Dashed curves give the results of numerical simulations.*

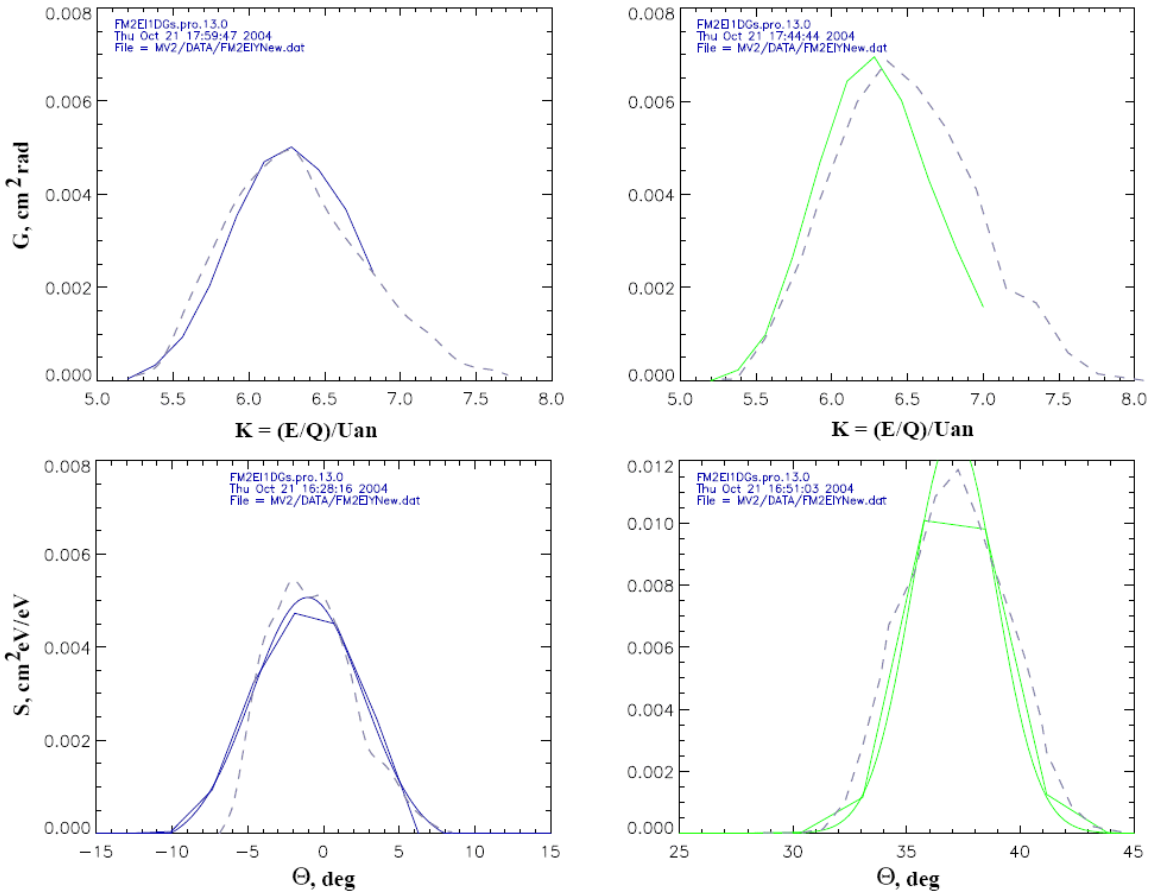

Figure 15: *Same as Figure 14 but for a "positive" sensor position (see Annex 3). Left column of the panels show properties for D = -0.077, and right panels correspond to D = 0.677.*

8. D-Elevation properties of the sensor

D - *Θ* properties have been obtained in experiments A and B (see Figure 10). In all cases measurements have been made for an azimuthal angle corresponding to the maximum count of a given sector for the "negative" sensor setup and to the maximal count of the 12th azimuthal sector for the "positive" setup.

However, later in the calibration procedure, the effective aperture of the sensor has been recalculated with respect to the 1st azimuthal sector to keep a continuous geometrical factor profile. The main results of these measurements are shown in Figures 16 and 17. Each profile corresponds to a specific D0 value. A number giving the line number in the resulting Table 2 marks each profile.

Each profile is the "effective aperture" *S* (see Annex 3) integrated over the energy response of the sensor for a given Θ (note that the azimuthal angle is constant). Thin curves show the Gaussian fit of the instrument responses. This fit simplifies the calculation of the G*lin* values. Note the strong asymmetry of ΔΘ for positive and negative elevations.

Figure 18 show the simulation results to be compared with the measurements.

A relative degradation of the experimental effective aperture versus the theoretical one is apparent for high elevations. This could be explained by the entrance grid interference and grid support interference (see Figure 24).

The main limitation of the instrument is clearly apparent: the range of possible elevation angles is limited to: -57° to +60°.

Another important result is the *D* versus Θ_M function which allows to calculate the needed electrode voltages to reach a given elevation angle. This profile is shown in Figure 19. There is a good agreement between theoretical and experimental values. Finally the D-Θ_M functions are given below:

$$\Theta_M = 3.04 + 81.5 \times D0 - 0.943 \times D0^2 \quad (9)$$

$$D0 = -3.74 \times 10^{-2} + 1.23 \times 10^{-2} \times \Theta_M + 1.81 \times 10^{-6} \times \Theta_M^2 \quad (10)$$

These functions are practically linear in the valid range of the elevation angles.

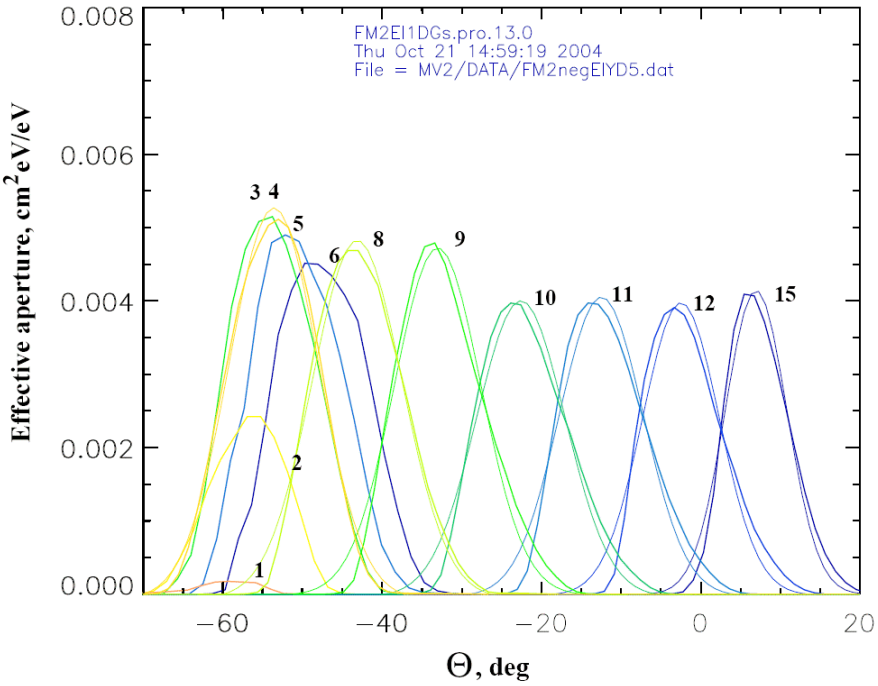

Figure 16: *Effective aperture versus the Θ angle for several D0 (and corresponding Θ_M) values, measured for the "negative" sensor setup (see Annex 3). Thin lines show the Gaussian fit of the profiles. Details of each profile including the exact position of the medium elevation angle and the corresponding* D0 *can be found in Table 2. The numbers on the curves in the figure correspond to the line numbering of Table 2*

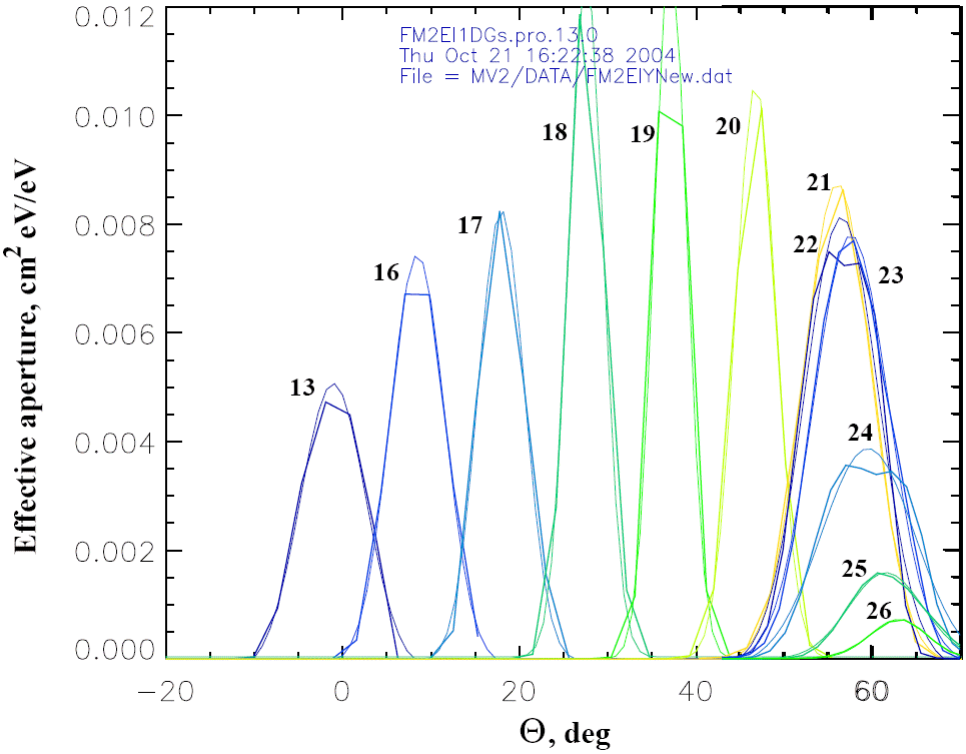

Figure 17: *Same as Figure 16 but for the "positive" sensor setup.*

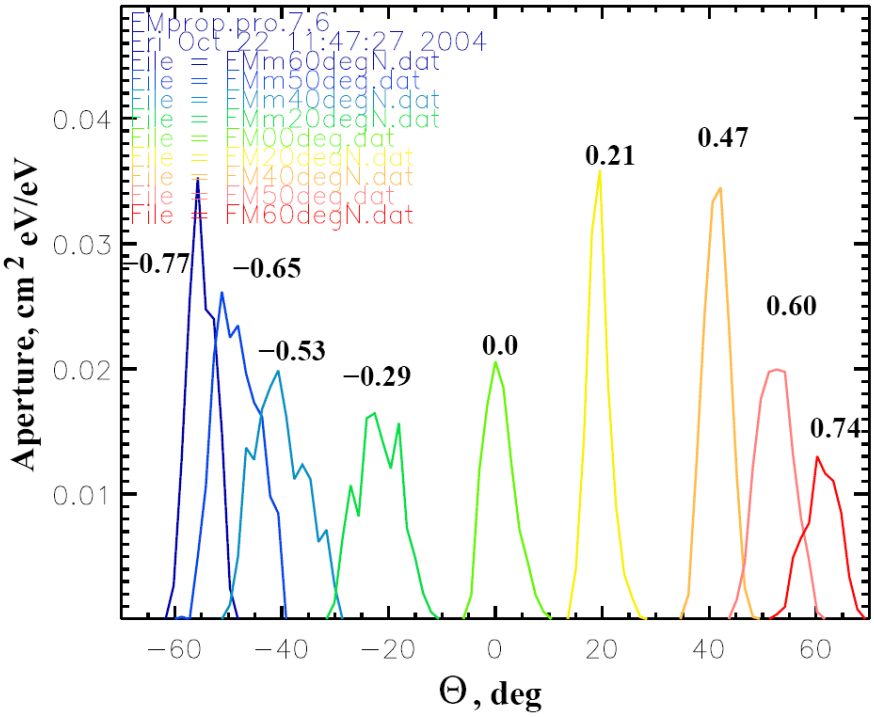

Figure 18: *Same as Figure 16 but for simulations results*

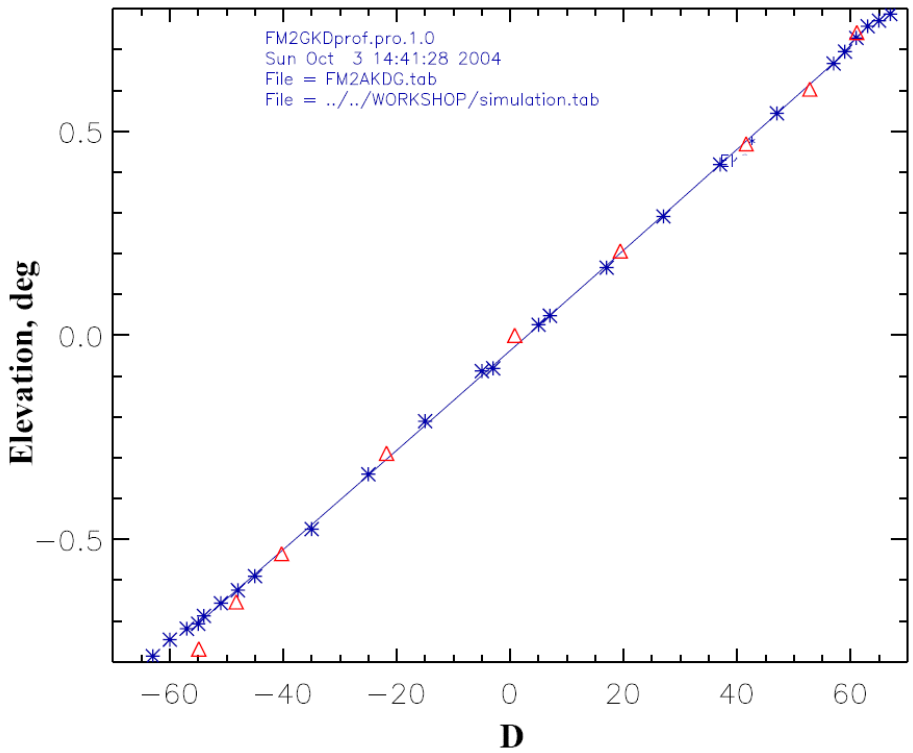

Figure 19: Θ_M *versus* D0. *Blue asterisks show experimental points. The solid line corresponds to the best fit of the experimental points (see text). The red triangles indicate the result of the sensor simulation (see Annex 4).*

9. Sensor properties versus elevation angle for a given azimuthal direction.

This section gives the variation of the main properties of the sensor versus the elevation angle for constant azimuths. The geometrical factor density (Glin) versus elevation is shown in Figure 20. It worth to note that for the data presented in Figures 17 – 22, there is no difference between Θ_M and Θ. Measurements are consistent with the simulation results if the efficiency of the sensor (grids, MCP, etc.) is 0.31. The geometrical factor can be described as:

$$\text{Glin [cm}^2\text{. rad. eV/eV]} = 8.80 \times 10^{-4} - 1.15 \times 10^{-7} \times \Theta + 1.25 \times 10^{-7} \times \Theta^2 \qquad (11)$$

Figure 21 shows the variation of the K0 factor versus Θ_M. Note the good agreement with simulation data. K0 can be expressed as:

$$K = 6.42 - 9.32 \times 10^{-4} \times \Theta - 5.52 \times 10^{-5} \times \Theta^2 \qquad (12)$$

The $\Delta E/E$ value is slightly less than the predicted one. It is expressed as:

$$\Delta E/E = 0.160 - 3.05 \times 10^{-6} \times \Theta \qquad (13)$$

Finally the width of the elevation response $\Delta\Theta$ versus Θ is shown in Figure 23. Note that $\Delta E/E$ and $\Delta\Theta$ are calculated as integral under the curve divided by the curve maximum. A Gaussian best fit has been used to calculate the integral and the maximum of the response. The width of the elevation response measured in "positive" and "negative" setups differ by almost 2°. This can be related to different steps of the *D* sweep or to the difference between the 3nd and the12th azimuthal sectors.

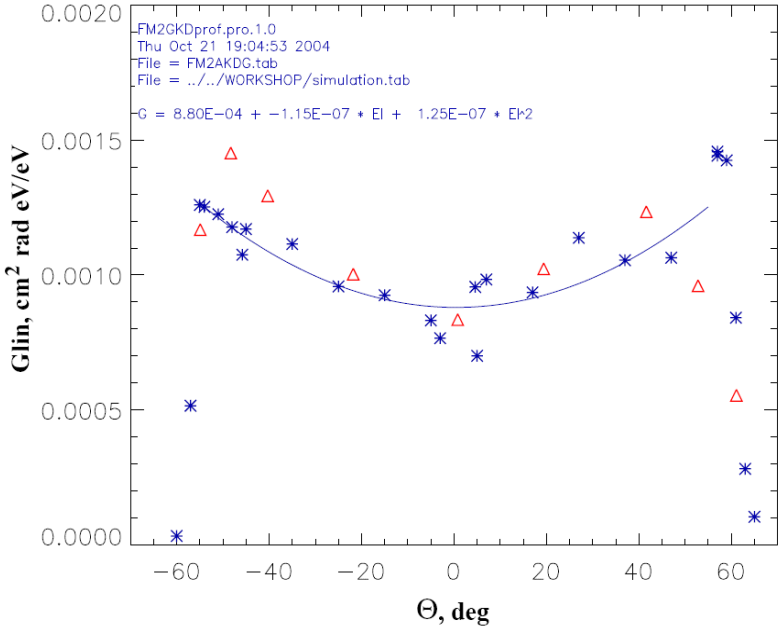

Figure 20: *G_{lin} profile versus elevation angle measured for a fixed azimuthal angle corresponding to the middle of the first azimuthal sector. Blue asterisks are experimental values and red triangles show results of the numerical simulation taken with a factor 0.17 (cf. Annex 4)*

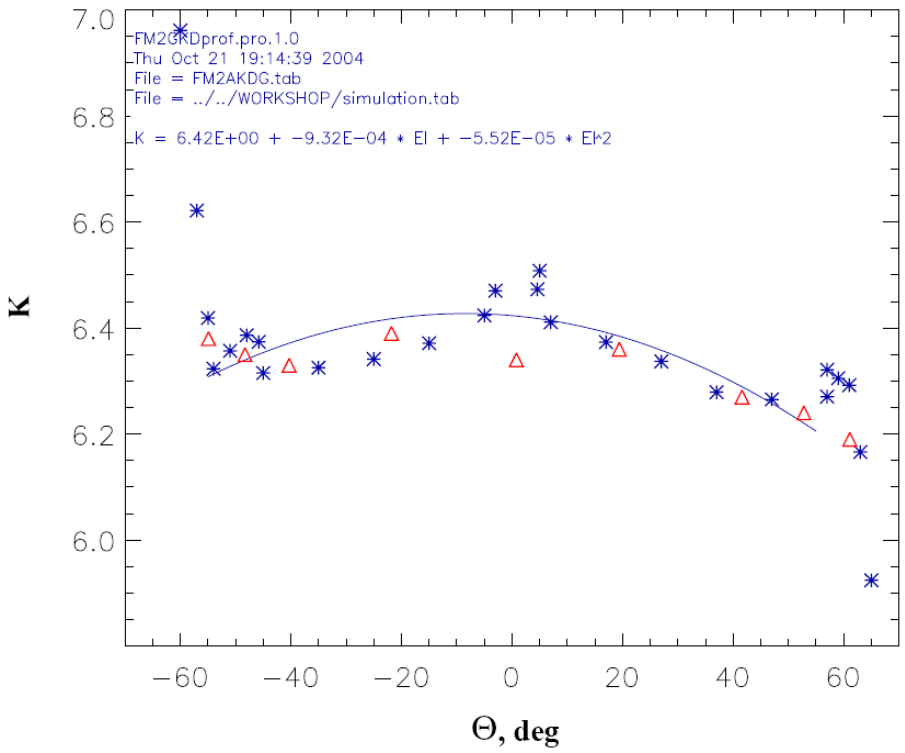

Figure 21 : *K versus elevation measured for an azimuth corresponding to the center of the 1st azimuthal sector.*

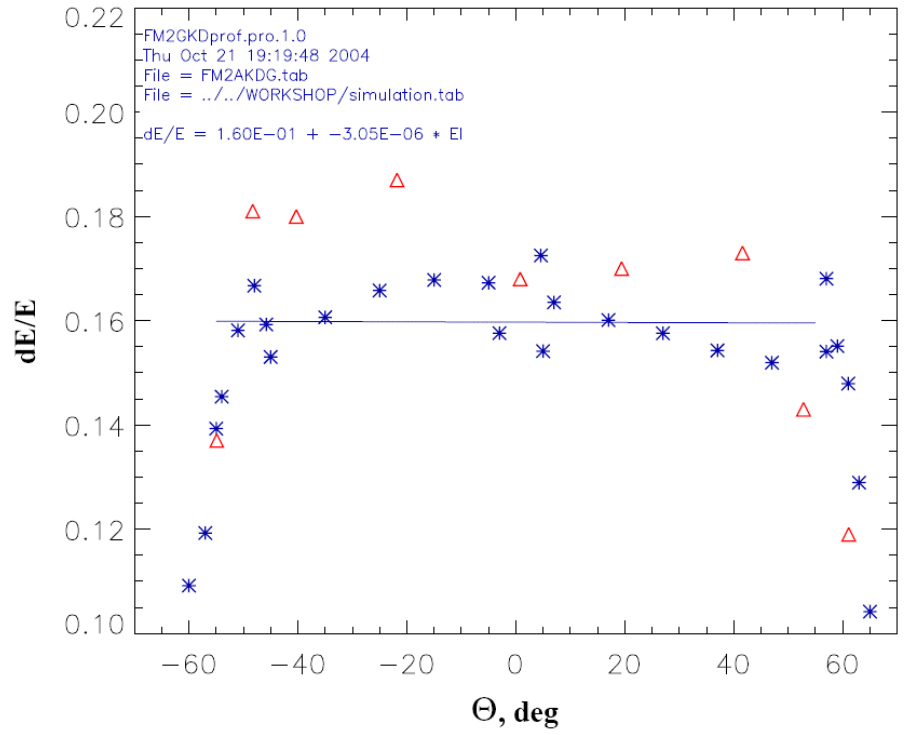

Figure 22 *: ΔE/E versus elevation angle. Conditions are the same as for Figure 21*

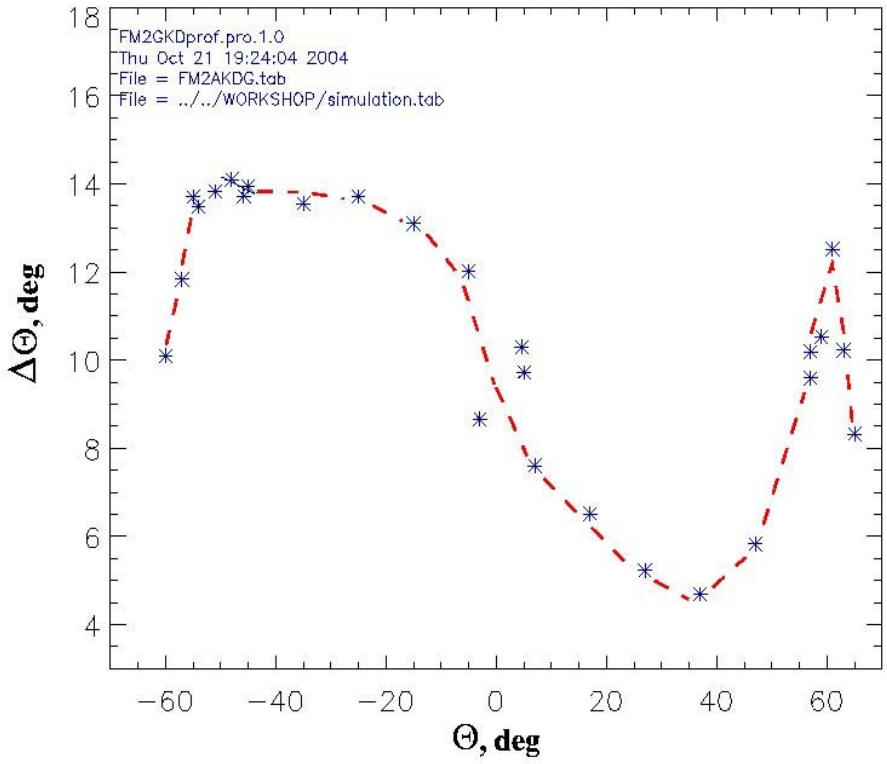

Figure 23: *Elevation response width versus elevation angle. Conditions are the same as for Figure 21*

N	Θ deg	D	ΔΘ, deg	K	ΔE/E	GF dens.cm^2 *rad eV/eV*
1	-60.0	-0.737	10.1	6.96	0.109	3.31 E-05
2	-57.0	-0.714	11.8	6.62	0.119	5.16 E-04
3	-55.0	-0.700	13.7	6.42	0.139	1.26 E-03
4	-54.0	-0.685	13.5	6.32	0.145	1.25 E-03
5	-51.0	-0.655	13.8	6.36	0.158	1.23 E-03
6	-48.0	-0.625	14.1	6.39	0.167	1.18 E-03
7	-45.8	-0.593	13.7	6.37	0.159	1.07 E-03
8	-45.0	-0.597	13.9	6.32	0.153	1.17 E-03
9	-35.0	-0.473	13.5	6.33	0.161	1.11 E-03
10	-25.0	-0.358	13.7	6.34	0.166	9.57 E-04
11	-15.0	-0.231	13.1	6.37	0.168	9.25 E-04
12	-5.0	-0.110	12.0	6.42	0.167	8.32 E-04
13	-3.0	-0.096	8.7	6.47	0.158	7.66 E-04
14	4.6	0.009	10.3	6.47	0.172	9.56 E-04
15	5.0	0.014	9.7	6.51	0.154	7.01 E-04
16	7.0	0.030	7.6	6.41	0.164	9.83 E-04
17	17.0	0.154	6.5	6.37	0.160	9.35 E-04
18	27.0	0.283	5.2	6.34	0.158	1.14 E-03
19	37.0	0.415	4.7	6.28	0.154	1.05 E-03
20	47.0	0.546	5.8	6.27	0.152	1.06 E-03
21	57.0	0.680	9.6	6.27	0.154	1.46 E-03

22	57.0	0.667	10.2	6.32	0.168	1.44 E-03
23	59.0	0.701	10.5	6.31	0.155	1.42 E-03
24	61.0	0.735	12.5	6.29	0.148	8.42 E-04
25	63.0	0.764	10.2	6.17	0.129	2.82 E-04
26	65.0	0.783	8.3	5.92	0.104	1.04 E-04

Table 2: *Summary table of SWEA properties for a specific azimuthal angle corresponding to the center of the first azimuthal sector*

11. Sensor properties as a function of the azimuthal angle for several elevations.

The effect of the grid support on the sensor transmission has been evaluated. The comparison of such a sector Φ-response with numerical simulations is shown in Figure 24.The grid support reduces the geometrical factor of the sector and changes the profile of the acceptance. This is especially important for high elevations (right panel). Thus this sector azimuthal response never has a flat part and its maximum is shifted from the support location.

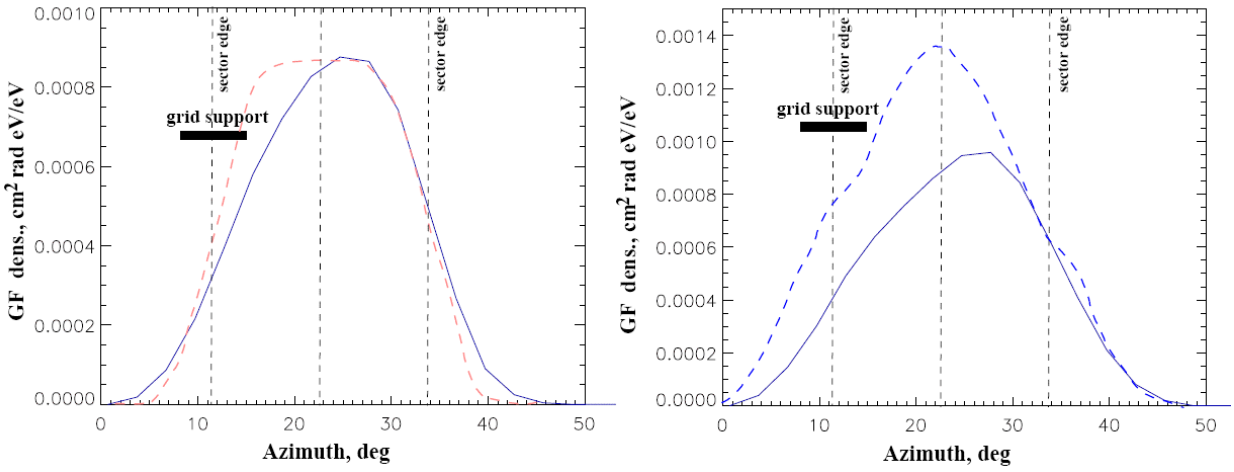

Figure 24: *Comparison of simulated and measured Glin for* $\Theta_M = 0°$ *(left panel) and* $\Theta_M = -45.8°$ *(right panel). In both cases the simulated Glin has been plotted with a reduction factor of 0.17.*

As mentioned in section 5, the azimuthal properties of the sensor for several specified elevation angles was measured. For each setup, namely "negative" and "positive", such a measurement has been done for elevations of ~50° and ~0°. Thus the measurements without deflection for two different setups can be compared (and for two different electron guns). The result of such a comparison is shown in Figure 25.

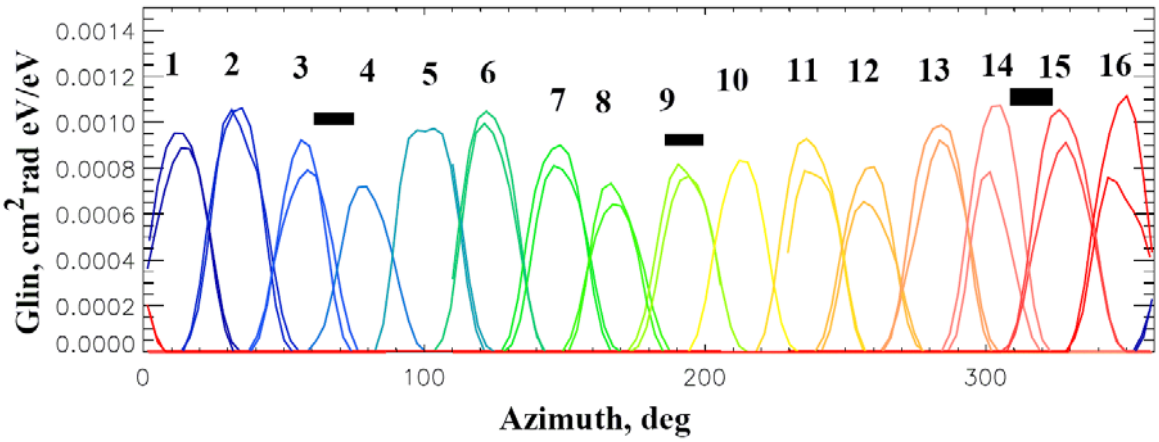

Figure 25: *Glin for D0 ~ 0 measured for the "negative" and the "positive" setups. Note the good consistency between the measurements except for sectors shadowed by the mechanical supports in case of "negative" setup (shown by black rectangles).*

Complete test results are shown in Figures 26, 27, 28, and in Tables 3, 4, 5, and 6.
Glin [cm^2.rad . eV/eV] versus the azimuth angle is shown in Figure 26 for four different elevations. The integration of Glin over the azimuth for each azimuthal sector gives the full geometrical factor of each sector. These geometrical factors are given in the Tables 3, 4 and 5. The other figures show the variations of *K* and *D* versus azimuth. These variations can be described by the following expressions:

Θ_M = -45.8°: ("négative")

$$K = 6.40 - 5.91 \times 10^{-2} \times \sin(\Phi) - 3.03 \times 10^{-3} \times \cos(\Phi) \quad (15)$$

$$D = -0.59 - 1.34 \times 10^{-2} \times \sin(\Phi) - 3.51 \times 10^{-3} \times \cos(\Phi) \quad (16)$$

Θ_M = 4.6° ("négative"):

$$K = 6.45 - 4.13 \times 10^{-2} \times \sin(\Phi) + 4.6 \times 10^{-4} \times \cos(\Phi) \quad (17)$$

$$D = 0.018 - 2.42 \times 10^{-3} \times \sin(\Phi) - 1.97 \times 10^{-3} \times \cos(\Phi) \quad (18)$$

Θ_M = -2.5° ("positive"):

$$K = 6.46 - 6.48 \times 10^{-2} \times \sin(\Phi) + 1.27 \times 10^{-2} \times \cos(\Phi) \quad (19)$$

$$D = -0.069 - 1.41 \times 10^{-3} \times \sin\{\Phi) - 2.6 \times 10^{-4} \times \cos(\Phi) \quad (20)$$

Θ_M = 46.0° ("positive"):

$$K = 6.25 - 1.79 \times 10^{-2} \times \sin(\Phi) + 2.64 \times 10^{-3} \times \cos(\Phi) \quad (21)$$

$$D = 0.546 - 4.34 \times 10^{-3} \times \sin(\Phi) - 4.93 \times 10^{-3} \times \cos(\Phi) \quad (22)$$

Sector	Azimuth, deg	K	D	GF cm^2. sr. eV/eV
1	12.7	6.40	-0.595	2.65E-04
2	32.4	6.39	-0.599	2.72E-04
3	55.9	6.34	-0.604	—
4	77.9	6.31	-0.602	—
5	100.9	6.31	-0.603	2.92E-04
6	121.2	6.34	-0.602	2.94E-04
7	144.3	6.40	-0.597	3.07E-04
8	166.2	6.41	-0.591	2.58E-04
9	191.7	6.40	-0.583	3.43E-04
10	—	—	—	—
11	239.0	6.46	-0.578	2.78E-04
12	257.5	6.45	-0.574	2.76E-04
13	284.1	6.43	-0.575	3.36E-04
14	300.9	6.46	-0.586	2.30E-04 *
15	327.7	6.41	-0.587	3.00E-04
16	347.9	6.41	-0.591	2.55E-04

Table3: *Azimuthal properties of SWEA for* Θ_M *= -45.8° ("négative" setup).*

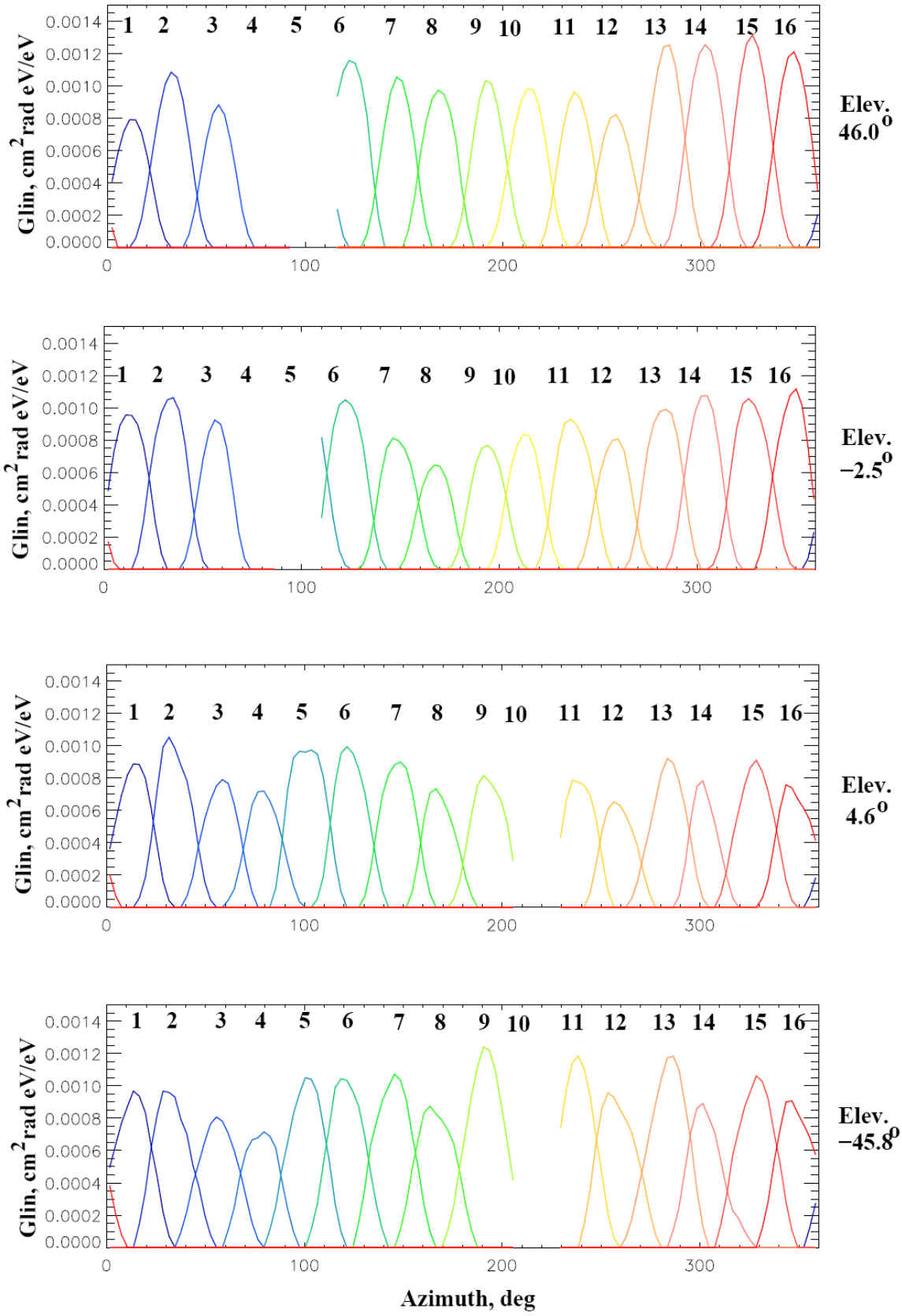

Figure 26: G_{lin} versus Φ for four different elevation angles. The two bottom panels correspond to the "negative" mechanical setup and the two top panels correspond to the "positive" mechanical setup. Numbers on the curves indicate the azimuthal sector number.

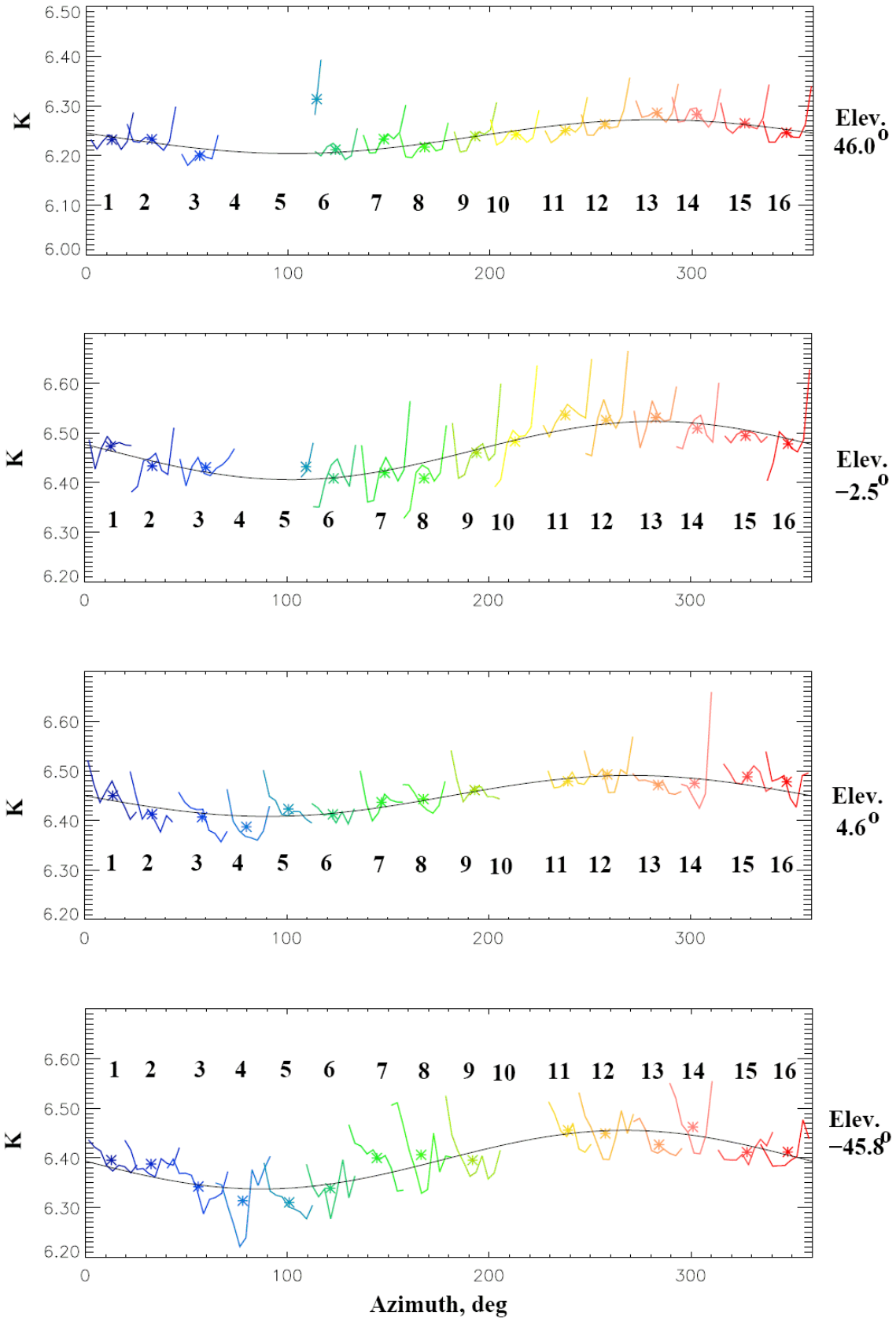

Figure 27: *K versus Φ for four different elevation angles. Layout is the same as in Figure 26*

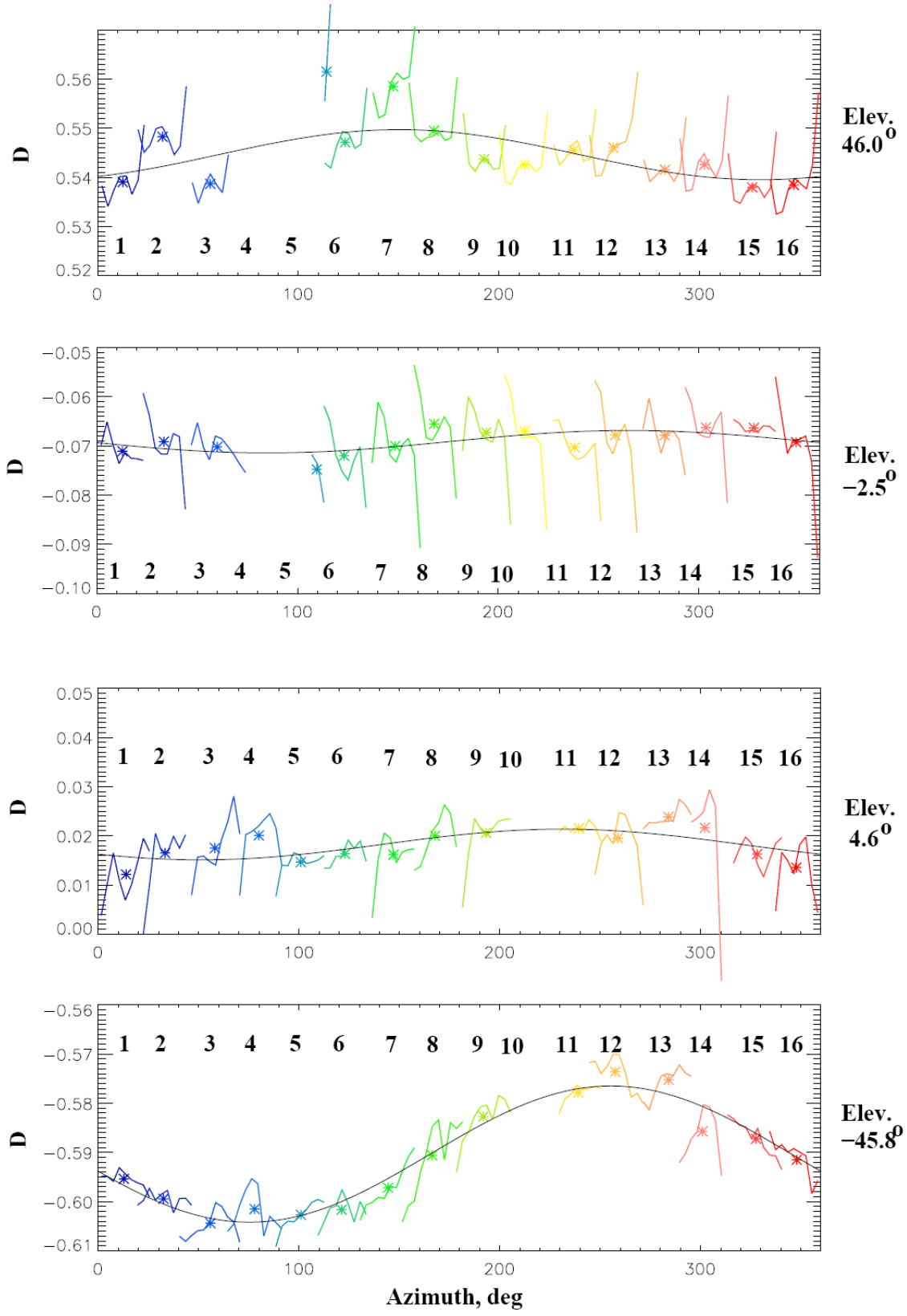

Figure 28: *D versus Φ for four different elevation angles. Layout is the same as in Figure 27*

Sector	Azimuth, deg	K	D	GF cm^2 *sr eV/eV*
1	13.8	6.45	0.012	3.35E-04
2	33.3	6.41	0.017	3.79E-04
3	58.1	6.41	0.018	—
4	80.0	6.39	0.020	—
5	100.9	6.42	0.015	4.05E-04
6	122.9	6.41	0.016	3.56E-04
7	147.0	6.44	0.016	3.39E-04
8	167.7	6.44	0.020	2.48E-04
9	193.1	6.46	0.021	3.02E-04
10	—	—	—	—
11	239.4	6.48	0.022	2.70E-04
12	258.8	6.49	0.020	2.32E-04
13	284.0	6.47	0.024	3.33E-04
14	302.1	6.47	0.022	2.20E-04
15	328.2	6.49	0.016	—
16	347.7	6.48	0.014	2.73E-04

Table 4: *Same as Table 3 but for* Θ_M *= 4.6° ("négative" setup)*

Sector	Azimuth, deg	K	D	GF *cm sr eV/eV*
1	12.7	6.47	-0.071	3.61E-04
2	33.4	6.43	-0.069	3.85E-04
A	56.4	6.42	-0.069	2.94E-04
4	109.6	6.43	-0.075	_____
5				
6	123.2	6.41	-0.072	3.94E-04
7	148.6	6.42	-0.070	3.00E-04
8	168.0	6.41	-0.066	2.24E-04
9	194.0	6.46	-0.067	2.77E-04
10	213.1	6.48	-0.067	2.91E-04
11	238.0	6.54	-0.070	3.54E-04
12	258.3	6.53	-0.068	2.81E-04
13	282.9	6.53	-0.068	3.73E-04
14	303.5	6.51	-0.066	3.79E-04
15	327.4	6.49	-0.066	4.13E-04
16	348.4	6.48	-0.069	3.83E-04

Table 5: *Same as Table 3 but for* Θ_M *= -2.5° ("positive" setup).*

Sector	Azimuth, deg	K	D	GF cm^2 *sr eV/eV*
1	12.6	6.23	0.539	1.97E-04
2	32.4	6.23	0.548	2.71E-04
3	56.2	6.20	0.539	1.96E-04
A				
4	114.1	6.31	0.561	__
5				
6	123.3	6.21	0.547	2.76E-04
7	147.3	6.23	0.558	2.42E-04
8	167.6	6.22	0.550	2.41E-04
9	192.6	6.24	0.544	2.40E-04
10	212.8	6.24	0.543	2.53E-04
11	237.2	6.25	0.546	2.24E-04
12	256.9	6.26	0.546	2.04E-04
13	282.7	6.29	0.542	3.06E-04
14	302.3	6.28	0.543	3.24E-04
15	326.2	6.26	0.538	3.24E-04
16	346.9	6.25	0.538	2.96E-04

Table 6: *Same as Table 3 but for* Θ_M *= 46.0° ("positive" setup).*